
Abstract

Theoretical condensed matter research is plagued by a fundamental issue of complexity. The sheer amount of degrees of freedom in a material on any technologically relevant scale is overwhelming (e.g. $\sim 10^{23}$ electrons per cm^3), and makes it impossible to describe the quantum mechanical wavefunction exactly.

The Hamiltonian plays a central role in the description of crystals, the subject of this thesis. It can be decomposed into various parts, and their interactions. Depending on the physics under scrutiny it then often suffices to solve only one of those parts. This can be either because the energy scales and associated timescales that govern the constituents are very different, or because the interactions between them are small. One example, often put into practice, is the separation of electronic and phononic (lattice) degrees of freedom, leading to the well-known Born-Oppenheimer approximation, decoupling their respective motion. Another is the often neglected spin-orbit coupling, due to the tiny prefactor associated with its relativistic origin.

Solving these subproblems then allows for progress to be made in understanding the physics that govern them. However, there will inevitably be systems for which this interaction is not small and leads to fascinating new physics that manifestly depends on both subsystems combined. In this thesis we focus on these cases and how they arise in functional materials, with the occasional eye towards applications in technology.

The reason why these cross-order couplings can be interesting for technological applications, is that often one of the orders is more robust with respect to perturbations, and therefore more long-lived, but also harder to control efficiently. By exploiting the cross-order coupling in certain materials, one could potentially control the long lived order by applying perturbations to the more easily controllable order.

In giant Rashba effect systems, the coupling between spin and ferroelectric order leads to a linear spin-splitting of the band structure, whose sign depends on the orientation of the ferroelectric polarization. We show that, rather than the relativistic Rashba effect, a combination of electrostatics and atomic spin-orbit coupling lies at the origin of the large splitting.

The coupling between magnetism and ferroelectricity in multiferroic GdMn_2O_5 leads to a never before observed four-state hysteresis loop for the ferroelectric polarization, which depends on the magnitude, angle and history of the applied magnetic field. As we will show, this four-state hysteresis loop is accompanied by a full 360° rotation of spins in the material, which resembles the crankshaft of a car, converting the linear back-and-forth motion of the magnetic field into a rotational motion of the spins.

In a thin film of elemental Chromium, the ultrafast dynamics of a spin density wave, coupled to a slower varying charge density wave, allows for a high degree of control of the latter through excitations of the former. This allows us to predict the sequence of optical pulses to be applied to the material in order to follow closely an enveloping signal function.

And finally, the coupling between ferroelectricity and strain in BaTiO_3 leads to a softening at purely ferroelectric domain walls, allowing for some mechanical control of the position of this wall.

We utilize both theoretical and computational tools to understand the nature of these interactions, how they lead to cross-order coupling in these materials, and how this then translates into the experimentally observed behavior.

Contents

1	Introduction	5
2	Theory	9
2.1	Spin-orbit coupling	9
2.2	Wannier Functions	9
3	Spin-momentum locking in high spin-orbit coupled ferroelectrics	13
3.1	Introduction	13
3.2	Rashba-Bychkov Effect	14
3.3	Orbital Rashba Effect	17
3.3.1	Tight-Binding model	17
3.4	Overview: Germanium Telluride	21
3.5	Methods	22
3.6	Band structure	22
3.7	Results and Discussion	24
3.8	Conclusions	25

Chapter 1

Introduction

Theoretical condensed matter research is plagued by a fundamental issue of complexity. The sheer amount of degrees of freedom in a material of any technologically relevant scale is overwhelming (e.g. $\sim 10^{23}$ electrons per cm^3), and make it impossible to describe the quantum mechanical wavefunction exactly [there is some more nice things along this line in Wen]. This forces researchers in the field to make approximations, as to make the problem tractable, while still capturing the essential physics resulting in the effects under investigation. The way to make progress with this undertaking has always been to try and isolate the parts of the system that play the biggest role in the effects under investigation, while neglecting those that only lead to more complexity.

As is well known, every quantum mechanical system is governed fundamentally by its Hamiltonian. One could go so far as to say that if we would be able to exactly calculate all of the eigenvectors and eigenvalues of the Hamiltonian describing the material under study, the field of condensed matter would be completed. This is ofcourse impossible for reasons stated before. The full Hamiltonian can be decomposed into contributions from all parts of the system, and interactions between those parts. It is then quite straightforward to separate these into different energy scales, or through $|\psi(t)\rangle = e^{-i\frac{\mathcal{H}t}{\hbar}} |\psi(0)\rangle$, different characteristic timescales. There are two alleys along which one can proceed to simplify the problem. When the interactions between these parts are negligible, the two subsystems can be decoupled and solved separately. This is, for example, the case in materials for which the relativistic spin-orbit coupling can be ignored, decoupling completely the spin and charge sectors of the Hamiltonian. The second way is when the interaction is not negligible, but the time scales are so different that for the description of the slow varying subsystem, the interaction with the fast moving one can be described by an average, time independent one, so-called mean-field approximations. Vice versa, the slow moving subsystem can be taken as static for the description of the fast moving one. An example of this is the well-known Born-Oppenheimer approximation that assumes the reaction of the electrons to displacements of the ions inside the material to be instantaneous.

Applying approximations like these systematically, allows to identify and approximately solve the important parts in order to describe many phenomena that present themselves in condensed matter. They form the backbone and starting point for further investigations gradually including more complexity to describe increas-

ingly complex physics.

This Thesis will discuss effects that depend crucially on these, usually negligible, interactions between two relatively well-understood subsystems. The three main interactions that will be discussed are: relativistic spin-orbit coupling (SOC), coupling charge and spin sectors of the Hamiltonian; Heisenberg magnetic exchange striction, coupling spins to atomic displacements (phonons); and electrostriction, where electric polarization leads to an associated strain texture.

Aside from the fundamental interest, technological development has always been a strong driving force in condensed matter research. Here too, the focus on interactions between subsystems can lead to beneficial discoveries, since it theoretically allows to influence one subsystem by applying a perturbation to the other. This can allow for more efficient or granular manipulation of, for example, magnetic order through applied currents or electric fields. Many success stories in this area led to leaps in technology, like the dramatic increase in density and efficiency of hard disks allowed for by the discovery of giant magnetoresistance [citation]. However, exactly due to the fact that in most cases these interactions can be neglected, it is often not easy to find materials where they are big enough to be effectively exploited for technological applications. It is therefore crucial to gain an intimate understanding what physics are at the base of these effects, in order to then try and optimize them. Here a selection of materials will be discussed in which the earlier mentioned interactions are larger, or behave in an unexpected fashion, in order to accomplish this deep understanding.

As mentioned before, SOC is a relativistic effect that can often be ignored if one is interested in the electronic structure of a crystal with light ions. When materials with heavier constituent ions are investigated, it often becomes important to include this effect either perturbatively, or even on equal footing to other contributions in the Hamiltonian. While, through the Kramers theorem [**Kramerstheorem**], this does not lead to the appearance of spin-polarized Bloch functions when inversion symmetry is present, in GeTe this symmetry is broken, however, and a linear spin-splitting develops away from time-reversal symmetric points in the first Brillouin Zone (BZ). This spin-splitting is usually attributed to the Rashba-Bychkov effect, which is a purely relativistic effect that can be derived through a $\mathbf{k} \cdot \mathbf{p}$ expansion of the effective electronic Dirac equation¹. However, as will be demonstrated in Chapter 3, another effect must lie at the origin in order to explain the properties of the observed spin-splitting. We will show that it is rather the combination of atomic SOC and the interaction of the orbital angular momentum of Bloch functions with the electric polarization, that causes the effect. From a technological standpoint, this large spin-splitting, which is dependent on the orientation of the electric polarization, can be used to not only generate spin-polarized currents, but also change sign of this spin-polarization by reversing the electric polarization using an external electric field. This can theoretically be exploited in a device first dreamt up by Datta and Das

¹Integrating out positrons by performing the Fouldy-Wouthuysen transformation

[Datta1990], i.e. a spin based field-effect transistor.

In Chapter ?? the focus will be shifted to the aspect of increased granularity of control over a lattice vibration through the excitation of a coupled spin density wave (SDW) in elemental Chromium. In this material a peculiar nesting of the fermi-surface results in the stabilization of the SDW, which in turn will optimize bondlengths between antiferromagnetically coupled ions to maximize the gained magnetic exchange energy. In essence, this leads to a shortening of bonds between ions with large spins, and lengthening those between small spins. This lies at the origin of the period lattice displacement (PLD) which can be probed using X-ray spectroscopy. As will be shown, by exciting the electronic subsystem that constitutes the SDW, the phonon associated with the PLD starts to oscillate due to diminished magnitude of the SDW. The electronic subsystem will then cool down partly restoring the SDW, while the phonon oscillation largely remains present due to the slow dynamics and low damping. By applying a sequence of excitations to the SDW, one can then achieve indirect, but incredibly granular control over the amplitude of the phonon mode. Moreover, this process allows for achieving excitation amplitudes that would not be possible if the phonon mode would be excited directly. [maybe this is not true?] The very fast (essentially instantaneous) dynamics of the SDW, and relatively strong coupling to the phonon mode with much slower dynamics, lies at the core of this behavior. While the technological relevance of this process is not immediately obvious, it does highlight the capabilities that a coupling between two orders with different dynamics can offer in terms of control, to the point where a pulse train can be designed using our model, such that the PLD oscillation follows a given envelope signal almost perfectly.

Chapter ?? continues with the discussion of a very peculiar example of a multi-ferroic material, namely, GdMn_2O_5 , and, more specifically, the very peculiar angular dependence of the magnetoelectric switching cycle that was experimentally observed. In this material, the geometric frustration between chains of the antiferromagnetically coupled Mn ions, and associated inversion symmetry breaking magnetic ground state, leads to a ferroelectric polarization. This is again due to magnetic exchange striction that shortens bonds with favorable spin orientations, and vice versa. An additional contribution to the electric polarization, from a similar origin, comes from the bonds between magnetic Gd and the neighboring Mn chains. This interaction is also frustrated, and due to the isotropic nature of the Gd spins, increases the total polarization significantly over other $R\text{Mn}_2\text{O}_5$ with R another rare-earth. This is another prime example where one can influence one order through excitation of another, allowing to switch the ferroelectric polarization by the application of an external magnetic field. In this chapter it will be shown that the switching behavior depends dramatically on the angle between the applied magnetic field and the crystalline a -axis. It turns out that three distinct switching regimes can be identified, with a never before observed four-state ² hysteresis loop forming the boundary

²Two low, and two high magnetic field states are cycled through.

between two neighboring two-state ³ hysteresis loops. This leads to the claim that this four-state loop is topologically protected (and distinct) in the sense that it will always exist as long as the two neighboring switching behaviors are present in a material. As will be shown, the behavior can be described through the use of a relatively simple semi-classical spin model, with the four-state behavior being present for a surprisingly large set of model parameters. Furthermore, from this model, we show that in the two-state behaviors the internal spins simply toggle back-and-forth between two states, whereas in the four-state switching half the spins perform a full 360° rotation through two up and down sweeps of the external magnetic field. This is a microscopic analogue of the crankshaft in a car, converting the linear up and down motion of the magnetic field (the pistons) into a unidirectional motion of the spins (the driveshaft). It will also be shown that the evolution of the energy landscape that lies at the origin of this behavior is very similar to that of a Thouless charge pump, more specifically to the one demonstrated in cold atom systems [Lohse16].

In the last chapter, the interaction between strain and ferroelectricity will be carefully studied in 180° domain walls in BaTiO_3 . As will be shown, while the domain wall is purely ferroelectric, i.e. it separates two domains with the same strain texture, it still appears mechanically softer under an applied force by a tip. It is not a priori clear why this occurs, since the wall is not ferroelastic. In ferroelastic domain walls one domain will be favored over another by the force applied through the tip, meaning that when it is applied to the wall, the tip will excite a very soft sliding domain wall mode. This mode is not present in either of the ferroelastic domains and thus the ferroelastic domain wall will appear softer. In our case, however, we show that also in purely ferroelectric domain walls, the interaction between the polarization and strain leads to the presence of a long range strain profile close to the wall. An atomic force microscopy tip applied to either side of the wall will interact with this strain profile, bending the wall towards it through the excitation of a similar sliding mode, which in turn makes it appear softer. This behavior allows to efficiently move ferroelectric domains (and domain walls) by applying a strain field through a tip. Seen as certain ferroelectric domain walls are conductive, this opens the door to manipulate conducting channels through the application of strain, something that could be used in electronic devices.

³One low, and one high magnetic field state.

Chapter 2

Theory

2.1 Spin-orbit coupling

2.2 Wannier Functions

In a lot of the work presented in this Thesis we construct simplified model Hamiltonians to describe the physics that result in a certain effect in real materials. For topics that deal with the electronic structure of materials, either directly in describing the Rashba-splitting of energy bands in Chapter 3, or indirectly to parametrize the magnetic exchanges between localized spins as in Chapter ??, a tight-binding model is the most appropriate tool. These are constructed using a limited set of local, atomic-like orbitals as the basis, which play the biggest role in the physics under investigation. Not only does this simplification make solving the numerics of the problem more tractable¹, the representation in terms of real-space localized wavefunctions over extended Bloch functions (BFs) often also leads to a more intuitive picture. There are two ways of proceeding in order to construct the tight-binding Hamiltonian. The first is to use a semi-empirical approach, where the elements of the Hamiltonian are written, using symmetry arguments, as combinations of certain model parameters, which in turn have to be fit to experiments. The second is to extract these parameters from a first-principles based simulation such as density functional theory. In thesis we favor the latter since it is more flexible, not depending on experiments while still providing quantitative results. This also allows for an easy comparison of multiple materials in order to better understand how certain physics manifest themselves in different cases.

The next obvious question then becomes how to choose a good set of localized orbitals. There are many ways to do this, but the one most natural for the purpose of describing the Hamiltonian of periodic crystals is that of the Wannier functions (WFs) [Wannier1937]. Constructing these functions (so-called Wannierization) implements the bridge between the extended plane waves that form the eigenstates of the Hamiltonian of a periodic crystal, and thus used in many first-principles DFT codes, and the limited localized basis set of the tight-binding model.

We will here give a short recap of the excellent review done by Marzari et. al.

¹A limited set of orbitals leads to a reduction of the dimensions of the matrices that represent various operators, lowering the computational cost.

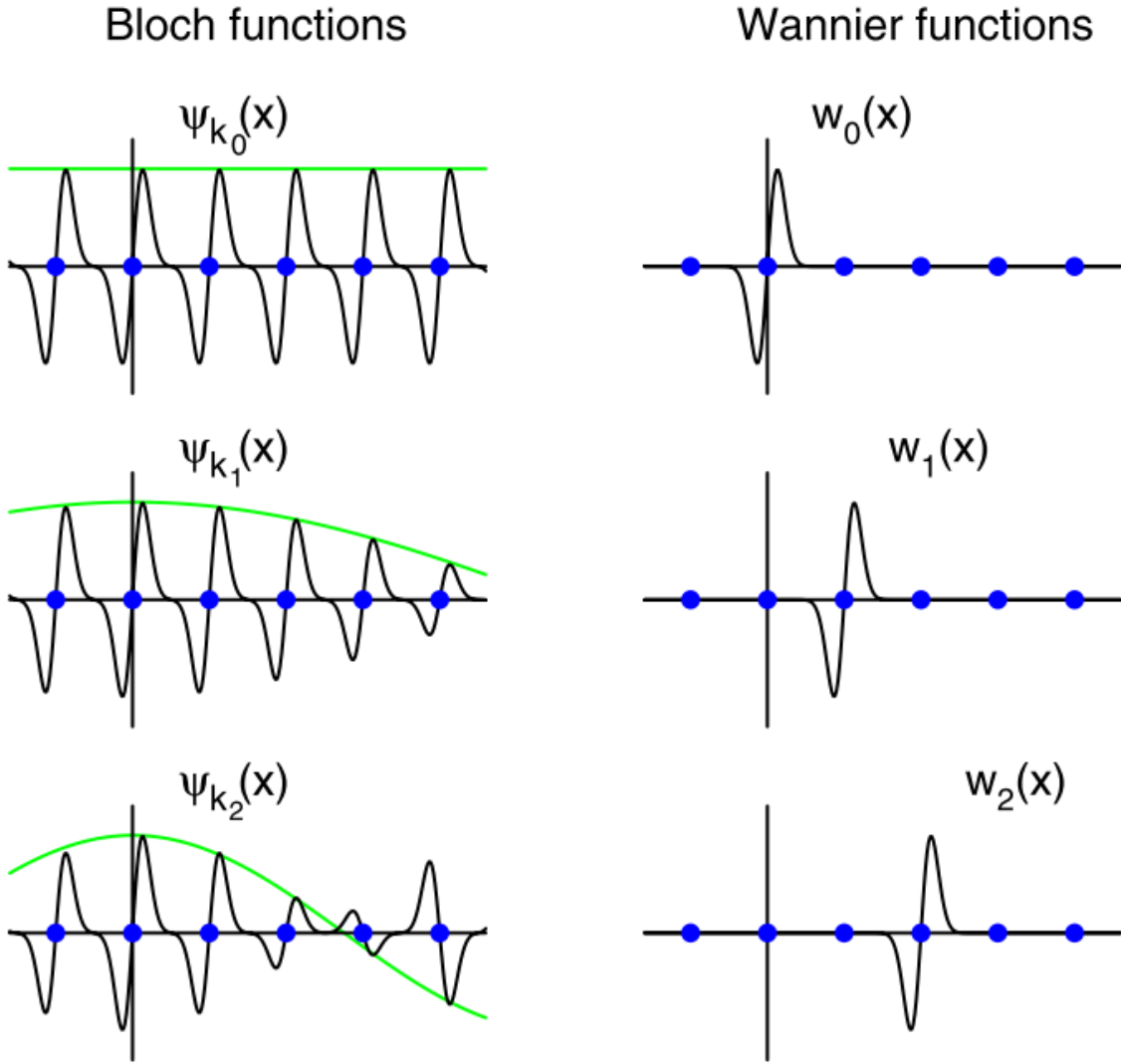


Figure 2.1

[Marzari2012].

The most clear case is that of a single, isolated band n with BFs $|\psi_{n\mathbf{k}}(\mathbf{r})\rangle$, where we can write the BF as a straightforward discrete Fourier transform of the WF:

$$|\psi_{n\mathbf{k}}(\mathbf{r})\rangle = e^{i\mathbf{k}\cdot\mathbf{r}} |u_{n\mathbf{k}}(\mathbf{r})\rangle = \sum_{\mathbf{R}} e^{i\mathbf{R}\cdot\mathbf{k}} |w_n(\mathbf{r} - \mathbf{R})\rangle, \quad (2.1)$$

with $|u_{n\mathbf{k}}(\mathbf{r})\rangle$ the periodic part of the BF, $|w_n(\mathbf{r} - \mathbf{R})\rangle$ the corresponding localized WF centered in the unit cell defined by lattice vector \mathbf{R} , and n the band index. The comparison between BFs and WFs is made in Fig. 2.1 taken from Ref. [Marzari2012]. In much of this work the term $e^{i\mathbf{k}\cdot\mathbf{r}}$ will be called the envelope (shown as the green graph), as it modulates the periodic $u_{n\mathbf{k}}$ part. When $k = 0$ we can see that the sum over the WFs, centered at different unit cells, reconstruct the $u_{n\mathbf{k}}$ periodic part of the BF. In the case of $k \neq 0$, similar to how the envelope part modulates the periodic part of the BF, the contribution of each WF to the total sum over the unit cells needs to be modulated in a discrete way through $e^{i\mathbf{k}\cdot\mathbf{R}}$.

The inverse Fourier transform over the BF in the first Brillouin Zone (BZ) can then be performed in order to generate the localized WF,

$$|w_n(\mathbf{r} - \mathbf{R})\rangle = \frac{V}{(2\pi)^3} \int_{BZ} d\mathbf{k} e^{-i\mathbf{k}\cdot\mathbf{R}} |\psi_{n\mathbf{k}}(\mathbf{r})\rangle, \quad (2.2)$$

where V denotes the real-space volume of the unit cell. In these and following equations, the normalization convention is used such that $\int_V d\mathbf{r} \langle \psi_{n\mathbf{k}}(\mathbf{r}) | \psi_{n\mathbf{k}}(\mathbf{r}) \rangle = 1$.

One of the most useful properties of the WFs lies in the realization that, through the gauge freedom at each \mathbf{k} of the BF², the shape of the WFs is not unique:

$$|\psi_{n\mathbf{k}}(\mathbf{r})\rangle \Rightarrow |\tilde{\psi}_{n\mathbf{k}}(\mathbf{r})\rangle = e^{i\phi_n(\mathbf{k})} |\psi_{n\mathbf{k}}(\mathbf{r})\rangle \quad (2.3)$$

$$|w_n(\mathbf{r} - \mathbf{R})\rangle \Rightarrow |\tilde{w}_n(\mathbf{r} - \mathbf{R})\rangle = \frac{V}{(2\pi)^3} \int_{BZ} d\mathbf{k} e^{-i(\mathbf{k}\cdot\mathbf{R} + \phi_n(\mathbf{k}))} |\psi_{n\mathbf{k}}(\mathbf{r})\rangle, \quad (2.4)$$

This means that by varying $\phi_n(\mathbf{k})$ we can adapt the used WF basis to the needs of the particular problem under investigation. In the case of a single isolated band, as discussed up to now, this is mainly a luxury. However, in most situations we are interested in groups of bands forming a composite manifold. In this case deciding the gauge in a good way

WFs offer a rigorous and flexible solution to this question, rewriting the BFs as a discrete Fourier transform of (exponentially) localized, cell-periodic wavefunctions.

This construction is flexible in the sense that it is not unique. BFs have a gauge freedom at each \mathbf{k} value, which in turn will have an effect on the WFs. One gauge that is commonly used is the one that localized the functions as much as possible, leading to the so-called Maximally Localized Wannier Functions (MLWF). Other gauges can be chosen such that the obtained functions have certain symmetries or have maximum similarity to atomic orbitals.

²The solution to Schrödinger equation does not depend on this phase.

Chapter 3

Spin-momentum locking in high spin-orbit coupled ferroelectrics

3.1 Introduction

The research field of spintronics aims to understand the behavior of spins inside materials, and translate this understanding into active control of these degrees of freedom for possible technological applications. Many possible devices have been theorized, for example, spin field-effect transistors (spin-FET)[1], and storage devices which utilize spin-current and associated spin-transfer torque to efficiently manipulate magnetic domains [7, 6]. In spite of fundamental interest and potential for applications, the actual realization of these devices has been rather elusive. One of the main culprits for the limited success to date is that the devices require very granular, ideally electric, control of the spin. This is often precluded by the widely separated energy scales and weak coupling between magnetic and charge degrees of freedom. One class of materials that can allow for such electric control of spin-polarized states are the ferroelectric semiconductors with large atomic spin-orbit coupling (SOC) [2, 5, 8]. Inversion symmetry breaking together with SOC results in a linear energy splitting of spin-polarized bands, manifested in the band structure as a conical intersection surrounding a time-reversal symmetric point of the Brillouin Zone (BZ) (see Fig. 3.1). Due to the definite spin-polarization of these bands, current carriers¹ traveling through the material will tend to align their spins to this spin-polarization. As we discuss in more detail in the following, the direction of the spin polarization depends on the orientation and strength of the electric field \mathbf{E} . In ferroelectrics, an internal field results from the polarization P , allowing it to be tuned and switched by an external electric field. These spin-polarized states have been observed both experimentally [5, 10, 9], and from *ab-initio* density functional theory (DFT) simulations [2]. It is, however, often not well understood and misattributed what the underlying microscopic mechanisms are that lead to the observed splitting.

We start by investigating multiple origins of this k and E dependent spin-splitting. The discussed energy contributions all arise due to the Hamiltonian of form

$$H_R(\mathbf{k}) = \alpha_R \frac{\mathbf{E}}{|\mathbf{E}|} \cdot (\mathbf{k} \times \hat{\sigma}), \quad (3.1)$$

¹holes in the case of Fig. 3.1

where $\hat{\sigma}$ is the electron spin operator, and \mathbf{E} the electric field. It will turn out that multiple microscopic effects can lead to contributions of this form, some of these are well known, others are more obscure. The magnitude of the contribution depends on the microscopic origin, namely whether the effect is purely relativistic or rather a combination of relativistic and electrostatic terms.

Certain materials showcase an exceedingly big splitting, for example in GeTe as can be seen in Fig. 3.1, and we therefore use this material as the main example throughout this chapter. To investigate how these effects occur in GeTe, we utilize DFT, followed by a Wannierization, in order to investigate local real-space properties of the Bloch functions around the time reversal symmetric points of the BZ.

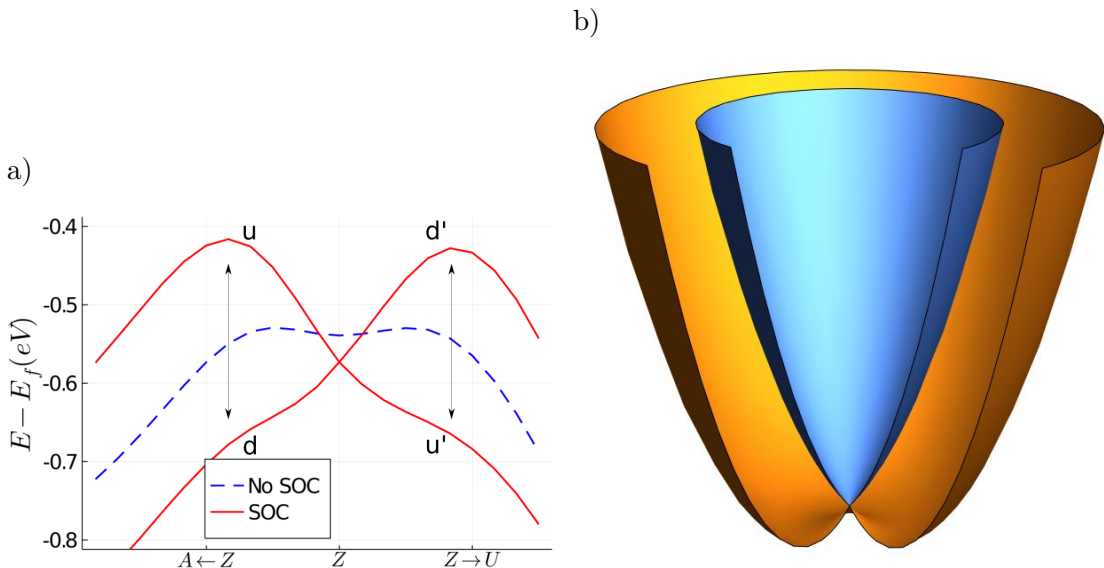


Figure 3.1: **Large Rashba splitting** (a) The band dispersion of the first valence band in GeTe, around the Z -point of the Brillouin zone (see Fig. 3.4 for details). Two graphs show both non spin-orbit coupled (NSOC, blue), and spin-orbit coupled (SOC, red) case. The $u-d$ and $u'-d'$ labels designate the up and down spin-polarized bands, where the prime signifies that the orientation of the spin axis depends on specific path followed in k -space. b) Shifted parabolic energy levels due to Rashba splitting, and associated spin texture.

We finish with a conclusion on the origin of most observed Rashba-like phenomena [could be better].

3.2 Rashba-Bychkov Effect

The first discovered and most well known effect bearing the form of Eq. 3.1 is the Rashba-Bychkov effect, first derived in their seminal 1959 paper[15]. It is a relativistic effect that is derived from an expansion to second order in $1/c$, c denoting the speed of light, of the electronic Dirac equation (where the Fouldy-Wouthuysen

transformation was applied):

$$\mathcal{H}\psi = \left[\frac{\mathbf{p}^2}{2m} - eV - \frac{e\hbar}{4m^2c^2}(\boldsymbol{\sigma} \cdot [\nabla V \times \mathbf{p}]) - \frac{\hbar^2}{8m^2c^2}\Delta V - \frac{\mathbf{p}^4}{8m^3c^2} \right] \psi = E\psi \quad (3.2)$$

where ψ is a two component spinor, V denotes the electric potential, $\boldsymbol{\sigma}$ a vector of Pauli-matrices ($\sigma_x, \sigma_y, \sigma_z$), m and e the electron mass and charge respectively, and \mathbf{p} the canonical momentum. The first two terms are the nonrelativistic part of the Hamiltonian, the third represents the SOC, the fourth is known as the Darwin effect and the fifth is the relativistic correction to the effective electron mass. As is common in literature, we introduce the spin-orbit coupling constant $\lambda = \frac{e\hbar}{4m^2c^2}$. In a crystal with a periodic potential $V(\mathbf{r})$, electronic wavefunctions are Bloch wavefunctions $\psi_n(\mathbf{k}, \mathbf{r}) = u_n(\mathbf{k}, \mathbf{r})e^{i\mathbf{k}\cdot\mathbf{r}}$, where u_n denotes the cell-periodic part, and n is the band index. To obtain the eigenvalue equation for $u_n(\mathbf{k}, \mathbf{r})$, we insert ψ_n in Eq. 3.2, and carry out the differentiation $\mathbf{p} e^{i\mathbf{k}\cdot\mathbf{r}} u_n(\mathbf{k}, \mathbf{r}) = e^{i\mathbf{k}\cdot\mathbf{r}}(\mathbf{p} + \mathbf{k})u_n(\mathbf{k}, \mathbf{r})$, and similarly $\mathbf{p}^2 \rightarrow (\mathbf{p} + \mathbf{k})^2$. This leads to the following equation for $u_n(\mathbf{k}, \mathbf{r})$:

$$E_n u_n(\mathbf{k}, \mathbf{r}) = (V_0 + V_1 + V_2 + V_3) u_n(\mathbf{k}, \mathbf{r}) \quad (3.3)$$

$$V_0(\mathbf{k}) = \frac{\mathbf{p}^2}{2m} - eV + \frac{\hbar^2 k^2}{2m} \quad (3.4)$$

$$V_1(\mathbf{k}) = \hbar \frac{\mathbf{k} \cdot \mathbf{p}}{m} \quad (3.5)$$

$$V_2(\mathbf{k}) = -\lambda \boldsymbol{\sigma} \cdot (\nabla V \times \mathbf{k}) \quad (3.6)$$

$$V_3(\mathbf{k}) = -\lambda \boldsymbol{\sigma} \cdot (\nabla V \times \mathbf{p}). \quad (3.7)$$

We neglected the last two terms of Eq. 3.2 since they are exceedingly small and don't contribute to the linear form of Eq. 3.1. It is important to understand how the electric fields inside the crystal contribute to V_2 and V_3 , where both terms originate from the application of \mathbf{p} to either $u_n(\mathbf{k}, \mathbf{r})$ or $e^{i\mathbf{k}\cdot\mathbf{r}}$, respectively. We first separate ∇V in two contributions, one coming from the potential wells created by the atoms, and another originating from the ferroelectric polarization (it is assumed that no external fields are applied):

$$\nabla V = \mathbf{E} = \mathbf{E}_{at} + \mathbf{E}_P \quad (3.8)$$

These contributions, together with the two parts of the Bloch functions (i.e. the cell periodic $u_n(\mathbf{k}, \mathbf{r})$, and envelope function $e^{i\mathbf{k}\cdot\mathbf{r}}$) are pictorially shown in Fig. 3.2.

Looking at the picture, it becomes clear that the contribution of the atomic potential applied to the envelope function is zero because while k is a constant, E_{at} is odd throughout the unit cell, leading to the contributions on either side of the potential well to cancel out. Thus the only contribution to the first term in Eq. 3.9 comes from the uniform (even) E_P , which in general is very small compared to the atomic one. A similar argument can be applied to the contribution to V_3 . Due to the shape of the periodic part of the wavefunction, only the contribution coming from

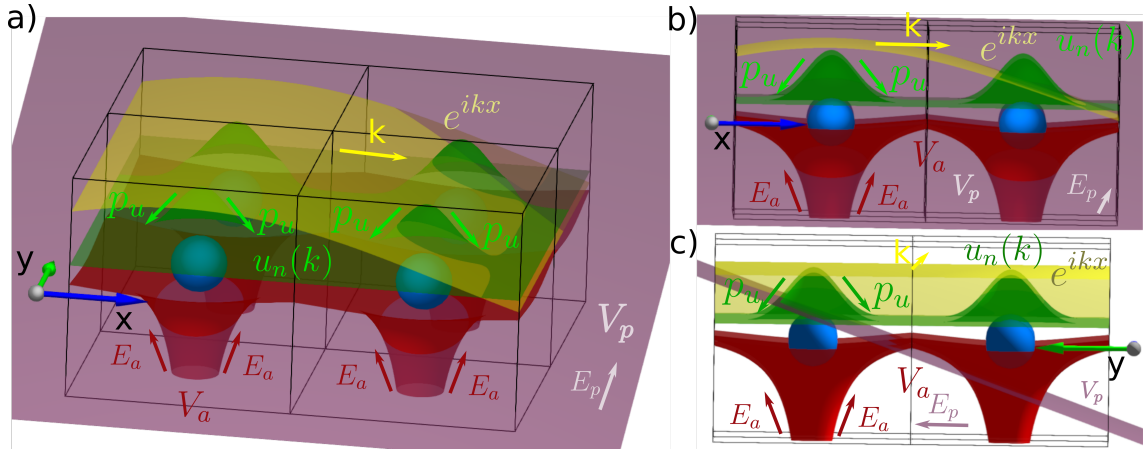


Figure 3.2: Pictorial representation of the different electric potentials (V) and fields (E) in a 2D square lattice. The blue spheres show the atoms, which produce the spherically symmetric red potential V_a and field E_a . The purple slab denotes a uniform ferroelectric polarization potential V_p which in this case is directed along the crystalline y -direction, creating field E_p . The green and yellow surfaces denote two components of the Bloch function: $u_n(k)e^{ikx}$, where the yellow is the envelope plane wave part and the green the cell periodic part. k and p_u denote the two components to the momentum of the bloch function, the former from the envelope function, and the latter the contribution from the periodic part.

E_{at} will be nonzero, this is essentially the well-known atomic spin-orbit coupling and can be rather large.

In the following it is assumed that Eq. 3.3 can be solved for a time reversal (TR) invariant point \mathbf{k}_0 in the first BZ, where the two spin states are necessarily degenerate. Due to the broken inversion symmetry and inclusion of the SOC terms (V_2, V_3), this degeneracy will be broken for k points away from the TR invariant point. We denote the two degenerate states at \mathbf{k}_0 by $|u_n^\downarrow\rangle$ and $|u_n^\uparrow\rangle$. It is important to realize that the orientation of spin axis of the eigenstates of Eq. 3.3 depends on the direction of both \mathbf{k} and \mathbf{P} , as will become clear later. Without loss of generality we take $\mathbf{k}_0 = \mathbf{0}$ and $E_n^{\uparrow,\downarrow}(\mathbf{0}) = 0$. Expanding in the deviation away from the high-symmetry point, in the usual $\mathbf{k} \cdot \mathbf{p}$ sense, and keeping only linear \mathbf{k} terms and terms up to second order in $1/c$, we get

$$E_n^{\sigma_1}(\mathbf{k}) = -V_2^{\sigma_1}(\mathbf{k}) + \quad (3.9)$$

$$\sum_{m,\sigma_2=\uparrow,\downarrow} \frac{\langle u_n^{\sigma_1} | V_1(\mathbf{k}) | u_m^{\sigma_2} \rangle \langle u_m^{\sigma_2} | V_3(\mathbf{k}) | u_n^{\sigma_1} \rangle + h.c.}{E_n^{\sigma_1} - E_m^{\sigma_2}}, \quad (3.10)$$

where the sum over m, σ_2 includes all states which are not equal to n, σ_1 .

Even though the latter term of Eq. 3.9 is of higher order in the perturbation theory, it usually has the same order of magnitude as the former. This can be understood from the previous discussion on the origin of various terms in Eq. 3.3, and in particular what fields contribute to V_2 or V_3 . For this to be true, however,

it is important that the orbitals u_n , and u_m in the second term have contributions that originate from an atom with a strong spin-orbit coupling. From the point of view of symmetries, another requirement for the second term to be nonzero is that u_n and u_m have contributions that have different parity, since \mathbf{p} is odd in spatial coordinates, $\mathbf{k} \cdot \mathbf{p}$ is only non-zero when one of the orbitals is odd with respect to a spatial direction and the other even. One example could be a p_y orbital and a $s-p_z$ hybridized one, which would be created by the ferroelectricity with electric polarization along the z -axis (add drawing? add hopping matrix?).

3.3 Orbital Rashba Effect

Unlike the purely relativistic Rashba-Bychkov effect, the orbital effect combines strong atomic SOC with the generation of nonzero orbital angular momentum (OAM) through electrostatic means. This contribution, therefore, is not limited by the small prefactors of Eq. 3.9. As will be explicitly shown below, electric dipole matrix element s can cause Bloch functions to acquire nonzero OAM when any electric field is present (e.g. from electric polarization), and vice versa Bloch functions with nonzero OAM acquire nonzero electric dipoles between unit cells[13, 12, 4]. This leads to two separate effects.

Firstly, when atomic SOC is included, OAM is unquenched at the high symmetry k -points. This leads to a correction to the band dispersion that varies linearly with \mathbf{k} . Secondly, even without including the contribution of the atomic SOC, the OAM of the Bloch functions to appear in a chiral texture as one moves away from the high-symmetry k -point, similarly to how the relativistic Rashba effect leads to a chiral spin texture. If one then includes the atomic SOC from Eq. 3.3, this linear-in- k l will lead to a linear variation of the energy with either positive or negative slope, depending on the spin orientation.

We now proceed by giving a pedagogical derivation of this mechanism based on a tight-binding model [13, 4].

3.3.1 Tight-Binding model

The tight-binding model is defined on a 2D square layer with one atom per unit cell, and four Wannier orbitals on the atom. We assume that these orbitals are gaussians the form $s(\mathbf{r}, \mathbf{n}) = e^{-\frac{|\mathbf{r}-\mathbf{n}a|^2}{a_0}}$, $p_\alpha(\mathbf{r}, \mathbf{n}) = \alpha e^{-\frac{|\mathbf{r}-\mathbf{n}a|^2}{a_0}}$ with $\alpha = x, y, z$, and \mathbf{n} denoting the unit cell indices $\mathbf{n} = (n_x, n_y)$. The reason for choosing gaussians is to make solving the overlap integrals more easy, it does not lead to any qualitative changes to the derivation below. To simplify notation below, we omit \mathbf{r} and write $|\alpha^0\rangle = |\alpha\rangle$. The bare tight-binding Hamiltonian is denoted as \hat{H}_0 and includes the usual hopping parameters due to overlap $t_{\alpha\beta}^{ij} = \int d\mathbf{r} w_i^\alpha(\mathbf{r})^* (\frac{\mathbf{p}^2}{2m} + V(\mathbf{r})) w_j^\beta(\mathbf{r})$. To mimick the inversion symmetry breaking in ferroelectric materials (i.e. with a polar space group), an electric field perpendicular to the layer (z direction) is applied.

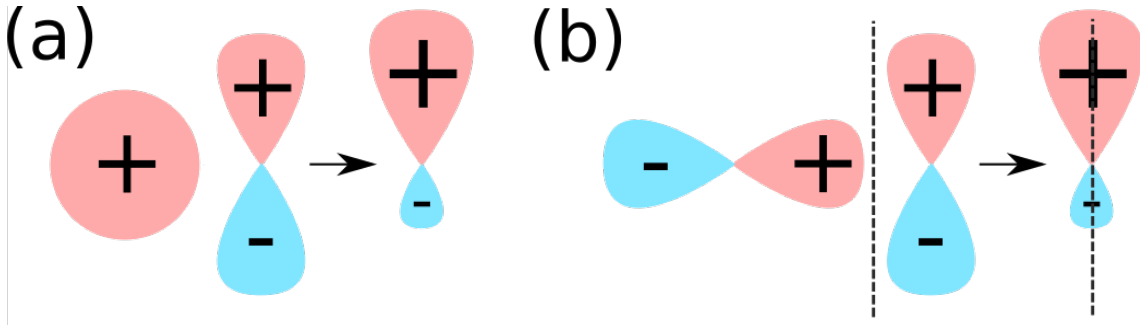


Figure 3.3: **Overlap dipoles.** (a) On-site dipole from s and p_z hybridization, (b) Dipole due to overlap of shifted p orbitals, the dashed line signifies a unit cell boundary.

This allows extra hopping terms associated with $\hat{H}_{isb} = e(\hat{\mathbf{d}} \cdot \mathbf{E})$, with $\hat{\mathbf{d}}$ the electric dipole moment:

$$\langle s | \hat{H}_{isb} | p_z \rangle = 2eE_z\theta_z^n \quad (3.11)$$

$$\langle p_z | \hat{H}_{isb} | p_x(\mathbf{n}) \rangle = eE_z\theta_z^n n_x \quad (3.12)$$

$$\langle p_z | \hat{H}_{isb} | p_y(\mathbf{n}) \rangle = eE_z\theta_z^n n_y \quad (3.13)$$

with $\theta_z^n = -ae^{-\frac{1}{2}\left(\frac{a|\mathbf{n}|}{a_0}\right)^2} \frac{\pi^{\frac{3}{2}}}{16\sqrt{2}}$, other terms of \hat{H}_{isb} are zero. Fig. 3.3 shows pictorially how these terms arise from the electric dipoles between the shifted orbitals.

Solving the tight binding model for $k = 0$, one can treat \hat{H}_{isb} as a perturbation on \hat{H}_0 due to the smallness of E_z , leading to a hybridization between the s and p_z orbitals:

$$|\tilde{p}_z\rangle = |p_z\rangle + \frac{\langle s | 2eE_z\theta_z^n | p_z \rangle}{\varepsilon_z - \varepsilon_s} |s\rangle \quad (3.14)$$

$$|\tilde{s}\rangle = |s\rangle + \frac{\langle p_z | 2eE_z\theta_z^n | s \rangle}{\varepsilon_s - \varepsilon_z} |p_z\rangle, \quad (3.15)$$

where $\varepsilon_s = \langle s | \hat{H}_0 | s \rangle$ and $\varepsilon_z = \langle p_z | \hat{H}_0 | p_z \rangle$. In order to proceed, we only treat the important kinetic energy part of \hat{H}_0 and rewrite it in terms of this hybrid \tilde{p}_z orbital in the central unit cell and the shifted p_x , p_y orbitals, leading to:

$$\langle \tilde{p}_z | \hat{H}_0 | p_x(\mathbf{n}) \rangle = \frac{2eE_z\theta_z^n}{\varepsilon_z - \varepsilon_s} \langle s | \frac{-\nabla^2}{2} | p_x(\mathbf{n}) \rangle \quad (3.16)$$

$$= \frac{4eE_z(\theta_z^n)^2}{\varepsilon_z - \varepsilon_s} n_x (-5 + a^2|\mathbf{n}|^2) \quad (3.17)$$

$$\langle \tilde{p}_z | \hat{H}_0 | p_y(\mathbf{n}) \rangle = \frac{4eE_z(\theta_z^n)^2}{\varepsilon_z - \varepsilon_s} n_y (-5 + a^2|\mathbf{n}|^2) \quad (3.18)$$

To construct $\hat{H}_0(\mathbf{k})$ and $\hat{H}_{isb}(\mathbf{k})$, one can Fourier transform the Wannier Functions:

$$|\alpha(\mathbf{k})\rangle = \frac{1}{\sqrt{N}} \sum_{\mathbf{n}} e^{i\mathbf{k}\cdot\mathbf{n}} |\alpha(\mathbf{n})\rangle \quad (3.19)$$

i with α one of the aforementioned orbitals, \mathbf{k} written in terms of crystalline coordinates ($\frac{2\pi}{a}$), and N denoting the total amount of unit cells in the material. This results in:

$$\hat{H}_0(\mathbf{k}) + \hat{H}_{isb}(\mathbf{k}) = \sum_{\mathbf{n}} e^{i\mathbf{k}\cdot\mathbf{n}} (\hat{H}_0(\mathbf{n}) + \hat{H}_{isb}(\mathbf{n})) \quad (3.20)$$

$$= \sum_{\mathbf{n}} i \sin(\mathbf{k} \cdot \mathbf{n}) (\hat{H}_0(\mathbf{n}) + \hat{H}_{isb}(\mathbf{n})) + k\text{-even terms}, \quad (3.21)$$

keeping only the $\sin(\mathbf{k} \cdot \mathbf{n})$ part of the exponent since the $\cos(\mathbf{k} \cdot \mathbf{n})$ part does not result in linear-in- k terms, in the small \mathbf{k} expansion below we keep only these linear-in- k terms.

If we then assume that at $k = 0$ the Bloch functions are formed from p_x, p_y, \tilde{p}_z and \tilde{s} orbitals: $|\alpha(\mathbf{k} = \mathbf{0})\rangle = \frac{1}{\sqrt{N}} \sum_{\mathbf{n}} |\alpha(\mathbf{n})\rangle$ a perturbation theory for small deviations \mathbf{k} away from zero can be written down:

$$|\alpha(\mathbf{k})\rangle = |\alpha\rangle + \sum_{\beta \neq \alpha} \frac{\langle \beta | H_0(\mathbf{k}) + \hat{H}_{isb}(\mathbf{k}) | \alpha \rangle}{\varepsilon_{\alpha} - \varepsilon_{\beta}} |\beta\rangle \quad (3.22)$$

Gathering the linear-in- k terms, and assuming $\varepsilon_p = \langle p_x | \hat{H}_0 | p_x \rangle = \langle p_y | \hat{H}_0 | p_y \rangle$, we find

$$|\tilde{p}_x(\mathbf{k})\rangle = |p_x(0)\rangle + \Theta \frac{ieE_z k_x}{\varepsilon_p - \varepsilon_{\tilde{z}}} |\tilde{p}_z(0)\rangle \quad (3.23)$$

$$|\tilde{p}_y(\mathbf{k})\rangle = |p_y(0)\rangle + \Theta \frac{ieE_z k_y}{\varepsilon_p - \varepsilon_{\tilde{z}}} |\tilde{p}_z(0)\rangle \quad (3.24)$$

$$|\tilde{p}_z(\mathbf{k})\rangle = |\tilde{p}_z(0)\rangle + \Theta \frac{ieE_z}{\varepsilon_p - \varepsilon_{\tilde{z}}} (k_x |p_x(0)\rangle + k_y |p_y(0)\rangle), \quad (3.25)$$

with $\Theta = \frac{\pi^{5/2}}{256a^3} \left(-16\sqrt{2} + \frac{3a\pi^{3/2}}{\varepsilon_z - \varepsilon_s} \right)$. Then, using the definition of the OAM operators for p -orbitals:

$$\hat{L}_x = \begin{pmatrix} 0 & 0 & 0 \\ 0 & 0 & -i \\ 0 & i & 0 \end{pmatrix}, \hat{L}_y = \begin{pmatrix} 0 & 0 & i \\ 0 & 0 & 0 \\ -i & 0 & 0 \end{pmatrix}, \hat{L}_z = \begin{pmatrix} 0 & -i & 0 \\ i & 0 & 0 \\ 0 & 0 & 0 \end{pmatrix} \quad (3.26)$$

we find that,

$$\langle \tilde{p}_z(\mathbf{k}) | \hat{L}_x | \tilde{p}_z(\mathbf{k}) \rangle = -2\Theta \frac{eE_z k_y}{\varepsilon_p - \varepsilon_{\tilde{z}}} \quad (3.27)$$

$$\langle \tilde{p}_z(\mathbf{k}) | \hat{L}_y | \tilde{p}_z(\mathbf{k}) \rangle = 2\Theta \frac{eE_z k_x}{\varepsilon_p - \varepsilon_{\tilde{z}}} \quad (3.28)$$

These expressions for $\hat{\mathbf{L}}$ can be filled into the expression for the atomic SOC $\hat{H}_{soc} = \lambda \hat{\mathbf{L}} \cdot \hat{\boldsymbol{\sigma}}$ to find the energy for $|\tilde{p}_z\rangle$:

$$\varepsilon(\mathbf{k}) = \frac{2\lambda\Theta eE_z}{\varepsilon_p - \varepsilon_{\tilde{z}}} (\mathbf{k} \times \boldsymbol{\sigma}) \quad (3.29)$$

which has the form of Eq. 3.1.

From this qualitative derivation, it is clear that the main reason behind the orbital Rashba effect can be traced back to the observation that Bloch functions with nonzero OAM have electric dipoles that couple to the inversion symmetry breaking electric field. We identified two sources that lead to the effect: the first one comes from the direct overlap dipoles between p_x and p_y orbitals, and the p_z orbital[13], the second is due to the hybridization of the s and p_z overlap, and the kinetic energy term between the s and neighboring p_x and p_y orbitals[4]. These two terms are reflected in the two terms that contribute to Θ , and lead to a chiral, linear-in- k texture of the OAM. If there then exists strong atomic SOC, this linear-in- k OAM will couple to the spin and result in the final Rashba-like form of Eq. 3.29.

There is one final term that contributes to the linear variation of OAM with \mathbf{k} , which is only present when there is an unquenching of the OAM at the high symmetry point ($|k| = 0$) due to the atomic SOC ???. This is due to the energy gain from \hat{H}_{soc} if the material has orbitals that have $\mathbf{j} = \mathbf{l} + \frac{1}{2}\boldsymbol{\sigma}$. Similar to the above derivation a small- k expansion for orbitals with nonzero OAM can be performed, leading in general to:

$$\langle \alpha | \hat{L}_\gamma | \beta \rangle = i\epsilon_{\alpha\beta\gamma} c_\alpha^* c_\beta \quad (3.30)$$

when α, β, γ designate x, y, z . This means that there has to be at least some admixing of multiple p -orbitals to get nonzero OAM. This leads to the following expansion of the Bloch functions around the high-symmetry $|k| = 0$ point:

$$|\psi(\mathbf{k})\rangle = \sum_{\mathbf{n}, \alpha} c_\alpha(\mathbf{k}) e^{i\mathbf{k} \cdot \mathbf{n}} |\alpha(\mathbf{n})\rangle \quad (3.31)$$

$$= \sum_{\mathbf{n}, \alpha} \left(c_\alpha(0) + \mathbf{k} \frac{\partial c_\alpha(\mathbf{k})}{\partial k} \Big|_{\mathbf{k}=0} \right) (1 + i\mathbf{k} \cdot \mathbf{n}) |\alpha(\mathbf{n})\rangle. \quad (3.32)$$

Focusing on the terms that vary linearly with k , the second term in the c expansion together with the first term in the exponent expansion is exactly the contribution that was discussed before. The final term for the Orbital Rashba effect originates from combining the first term in the c expansion with the second in the exponent expansion, leading to the contribution

$$\varepsilon(\mathbf{k}) = \langle \psi(\mathbf{k}) | \hat{H}_{isb} | \psi(\mathbf{k}) \rangle = i \sum_{\mathbf{n}, \alpha, \beta} c_\alpha^*(0) c_\beta(0) \mathbf{k} \cdot \mathbf{n} \langle \alpha(0) | \hat{H}_{isb} | \beta(\mathbf{n}) \rangle \quad (3.33)$$

$$= ieE_z \frac{-\pi^{5/2}}{8\sqrt{2}a^3} (c_x^*(0)c_z(0)k_x + c_y^*(0)c_z(0)k_y) \quad (3.34)$$

$$= eE_z \frac{\pi^{5/2}}{8\sqrt{2}a^3} (L_y(0)k_x - L_x(0)k_y). \quad (3.35)$$

These expressions show us that, due to $\hat{H}_{soc} = \lambda \hat{\mathbf{L}} \cdot \hat{\boldsymbol{\sigma}}$ and $\hat{H}_{isb} = eE_z d_z$, an additional Rashba-like term appears in the energy dispersion.

With the understanding that one can find Rashba like dispersions, coming not from the usually considered purely relativistic, but also from electrostatic mechanisms. We now look at a concrete example that behaves very similar to the above toy model, GeTe.

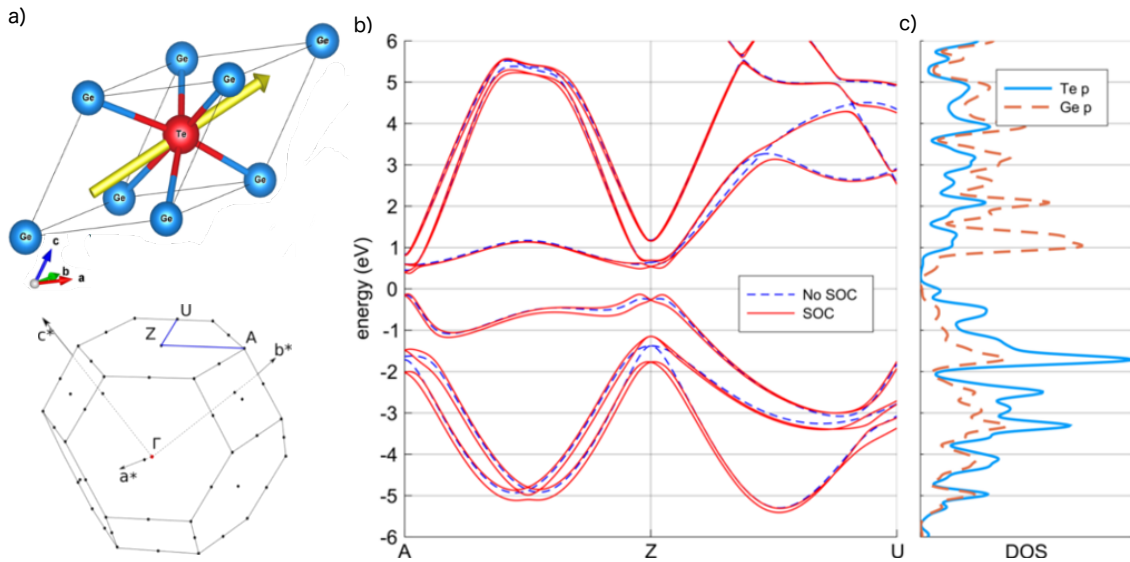


Figure 3.4: (a) Rhombohedral unit cell and Brillouin zone of GeTe, with the polarization direction in yellow. (b) Band structure obtained from a DFT calculation with and without SOC, along the blue path in panel (a). (c) partial DOS for Te and Ge p orbitals computed without SOC.

3.4 Overview: Germanium Telluride

The space group of GeTe is $R\bar{3}m$ (#160 in International Tables), with ferroelectric polarization along the threefold rotation z -axis caused by an off-centering of the central Te atom [14] as displayed in Fig. 3.4-(a). The valence and conduction bands are formed mostly by s and p orbitals from Te and Ge, respectively. This, together with the large spin-splitting in the vicinity of the Z point [2] as observed from the bandstructure in Fig. 3.4-(b), lends it as a perfect test-case for the above described mechanisms. Moreover, since it is a bulk material, the relativistic Rashba effects contribute negligibly due to the small potential gradients caused by bulk ferroelectricity. The band structure, presents a distinct large linear spin splitting around the Z point, along the $Z - A$ and $Z - U$ paths. The $Z - \Gamma$ path shows no splitting because the electric field is along the z direction, and as shown by the above derivation, only k_x and k_y will show a linear splitting. The density of states (DOS), displayed in Fig. 3.4-(c), confirms the orbital character of the bands.

3.5 Methods

We performed ab-initio DFT calculations using the Quantum-Espresso software package[3]. In order to confirm the linear varying OAM even when spin-orbit is not included we performed non-relativistic, as well as fully relativistic calculations. Both were performed using ONCVPSP pseudopotentials, with 30 Ry for the energy cutoff, and 120 Ry for the density cutoff. The reciprocal space was sampled using a 6x6x6 Monkhorst-Pack grid, for the self-consistent and non self-consistent calculations, using an energy convergence threshold of 10^{-7} Ry. Afterwards we used the Wannier90 package [11] to perform the Wannierization, using projections on atomic *s*- and *p*-orbitals for both Ge and Te ions. The result is showcased in Fig. 3.5.

Since the present theory depends crucially on local, real space, properties of the Bloch functions, the next step is to generate the Wannier orbitals $|w_\alpha(\mathbf{r})\rangle$.

This provides us with the tools to analyze the real space properties of Bloch functions such as the dipole moment and OAM.

3.6 Band structure

The bands we will focus on most are the three topmost valence bands. As seen in Fig. 3.4-(b), these bands have the largest spin-splitting. This suggests that indeed

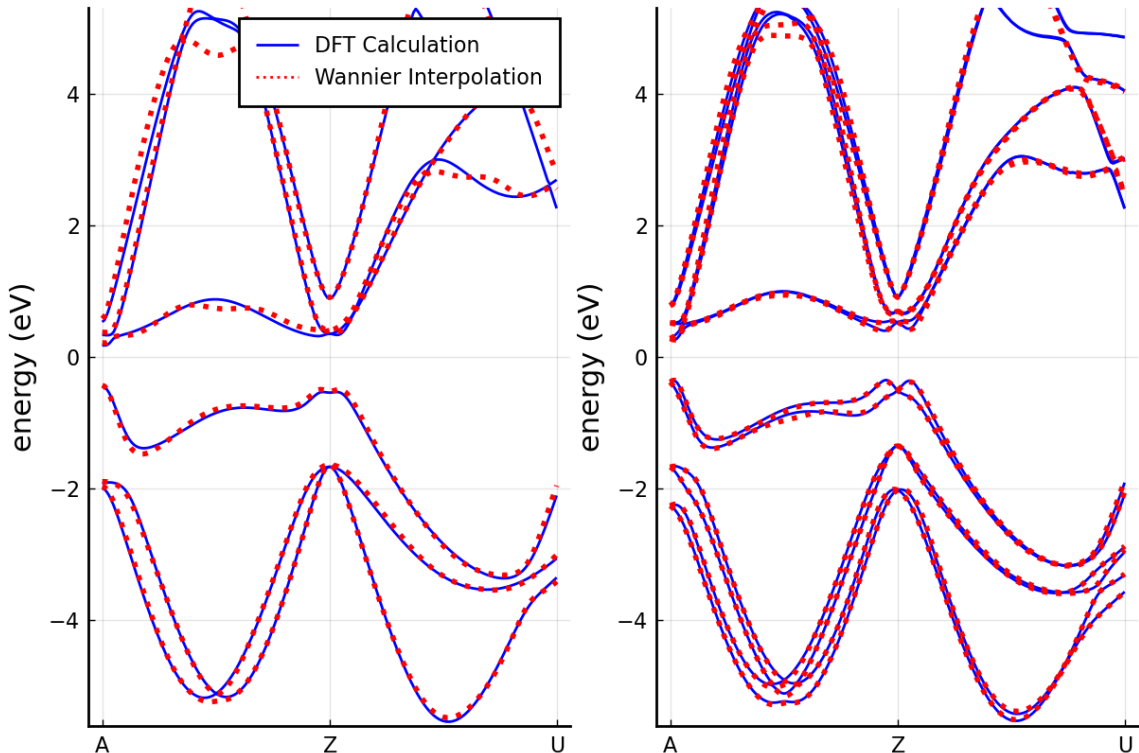


Figure 3.5: Result of Wannierization procedure for non-relativistic (a) and relativistic (b) calculations.

the atomic SOC plays an important role, seen as these bands are comprised mostly of Te orbitals, and SOC is largest on Te. If one were to fit the dispersion of the topmost band to Eq. 3.1, it results in a large prefactor $\alpha_R \approx 30.7 \text{ eV}\cdot\text{\AA}$ [2]. As discussed before, a more realistic prefactor would be $\alpha_R = 10^{-6} \text{ eV}$ in the purely relativistic case inside the vacuum.

The last issue with the purely relativistic explanation, which has been confirmed experimentally[9], lies in the orientation of the spin polarization of the split bands. According to Eq. 3.1, the bands should all be split equally and Bloch functions at the same k -point should have the same spin orientations, since their character does not enter Eq. 3.1. However, as has been shown and will be confirmed by our results

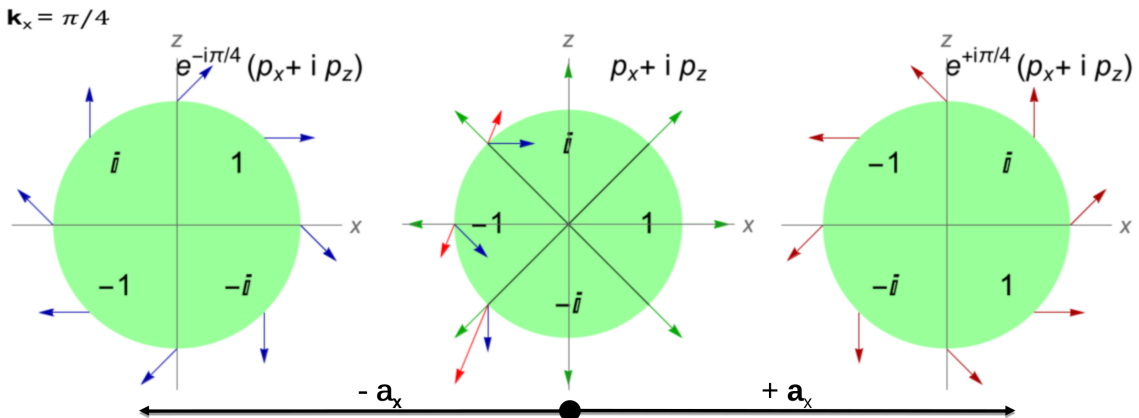


Figure 3.6: Interference between orbitals with nonzero OAM. Three neighboring unit cells are displayed, each with the same $p_x + ip_z$ orbital (thus having nonzero l_y). The wave functions of the left and right unit cells have their phase rotated by the plane-wave part $e^{ik_x R_x}$. The amplitude and phase of the wave function are encoded with the length and polar angle of the arrows.

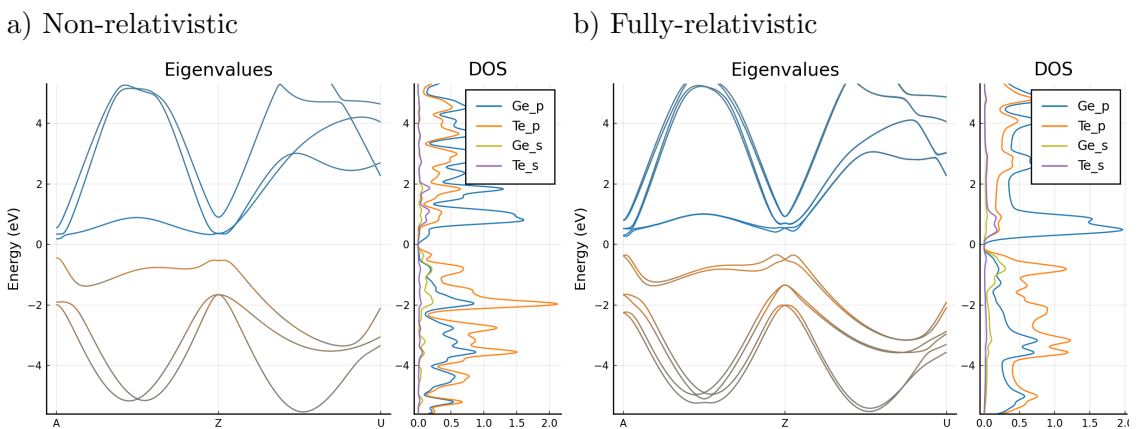


Figure 3.7: Bandstructure and projected density of states. In both panels the bandstructure was colored according to the contribution of the constituent orbitals, as indicated in the density of state plots. The bands that are formed by the s -orbitals are situated 5 eV below the shown window.

below, the orientation depends on the character of the band, more specifically on the value of the total angular momentum j .

3.7 Results and Discussion

The dispersion, OAM, and SAM of the first valence band are shown in the left panel of Fig. 3.8. Confirming our earlier conclusions, we can see that non-zero, linearly varying OAM is formed as we move away from the high-symmetry Z -point. Moreover, the OAM is perpendicular to both the z -axis and the k vector, as it should be from Eq. 3.27, and can also be seen from the panels in Fig. 3.10. This leads e.g. to $l_y = 0$ along the $A \rightarrow Z$ path, where only k_y is nonzero. When atomic SOC is included in the orange and blue graphs, we see the spin-splitting that results from having the spin oriented either along or opposite to the already linearly varying OAM. The unquenching of the OAM at the Z -point when SOC is included is also clearly visible, together with the resulting change in the slope that originates from the corresponding contribution to the dipole moment Eq. 3.33. This correlation can also be observed in the panel showing the center of mass $\bar{z} = \int_{\text{supercell}} z |\psi(k)|^2$ of the Bloch-functions, which is proportional to the dipole moment around the same reference point.

When we compare this first valence band with the third valence band, shown in the right panel of Fig. 3.8, we can clearly see the previously discussed issues with the purely relativistic explanation. As stated before, we can note that not only the magnitude but also the sign of the prefactor in Eq. 3.1 is opposite for these two bands, showcased by the size of the splitting, and by the ordering of the spin-up vs the spin-down splitted part. This is because the character of the first and third valence bands are different. The first valence band is mostly coming from Te $j_{\frac{3}{2}}$ orbitals, whereas the third valence band is predominantly $j_{\frac{1}{2}}$. This causes the orientation of the OAM and SAM to be along eachother in the first band, and opposite for the third, as shown in Fig. 3.10. This then leads to the different ordering of the spin-split bands.

There is one last very interesting feature one can notice from Fig. 3.10 (c) and (f), that is, the switching of the character (and SAM, OAM orientation) of the bands, very close to the Z point. This is because the crystal field breaks rotational symmetry causing the atomic j to not be a conserved quantity, i.e. there is a mixing between different atomic j orbitals, which varies strongly in this very narrow region around Z .

All these considerations lead to a very nontrivial SAM and OAM texture of the bands as we progress through the BZ.

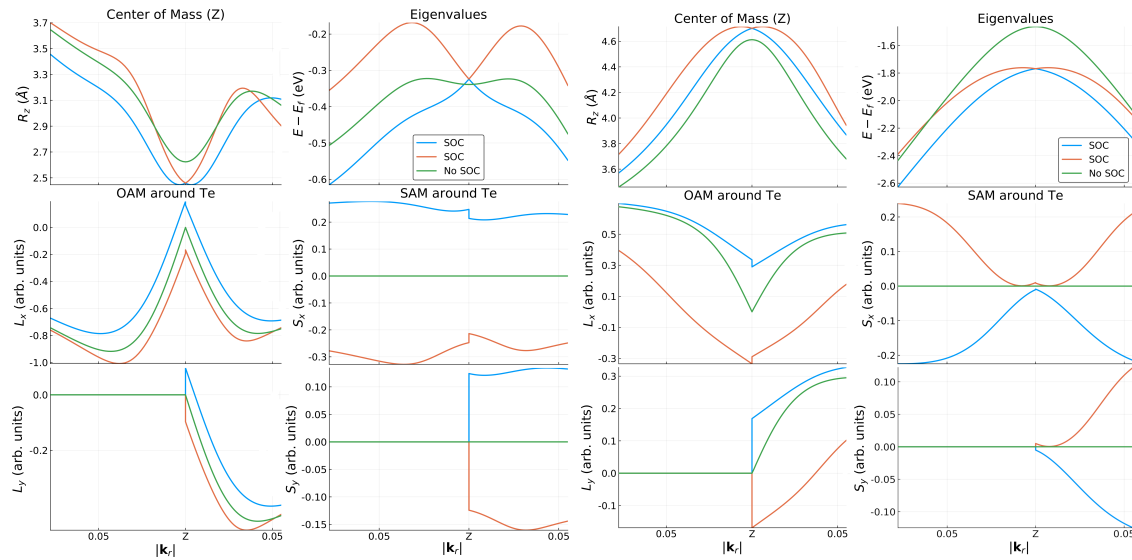


Figure 3.8: Comparison between the real-space observables and energy dispersion in (a) the first and (b) third valence band. The values are plotted in function of the relative distance from the Z point $\mathbf{k}_r = \mathbf{k} - \mathbf{k}_Z$, towards the A and U points. The green graphs denote the values before turning on atomic SOC, whereas the orange and blue graphs denote the two spin-split bands.

3.8 Conclusions

We have explored the microscopic origin of the giant Rashba-like spin splitting in the band structure of bulk ferroelectric GeTe with high atomic SOC. We derived the form of the band dispersion in the Wannier representation, that relates the large spin splitting to the intricate interplay between OAM, atomic SOC, the crystal field and the electric polarization. It turns out that the crucial component, which is not present in the relativistic Rashba effect, is the emergence of a nonzero electric dipole of the Bloch functions due to their OAM. The quantitative analysis based on Wannier functions and atomic-centered approximation confirms this mechanism in GeTe. We find a very good agreement between the proposed band dispersion, Eq. (??), and the dispersions of the first and third valence bands, where the effect manifests itself most clearly.

Ultimately, the results suggest that (1) large ferroelectric polarization, (2) high atomic SOC, and (3) highly symmetric environment producing little OAM quenching could be the design rules for new materials with strong Rashba-like spin splitting. These materials could enable spintronic devices with the much needed electric control of spin polarization.

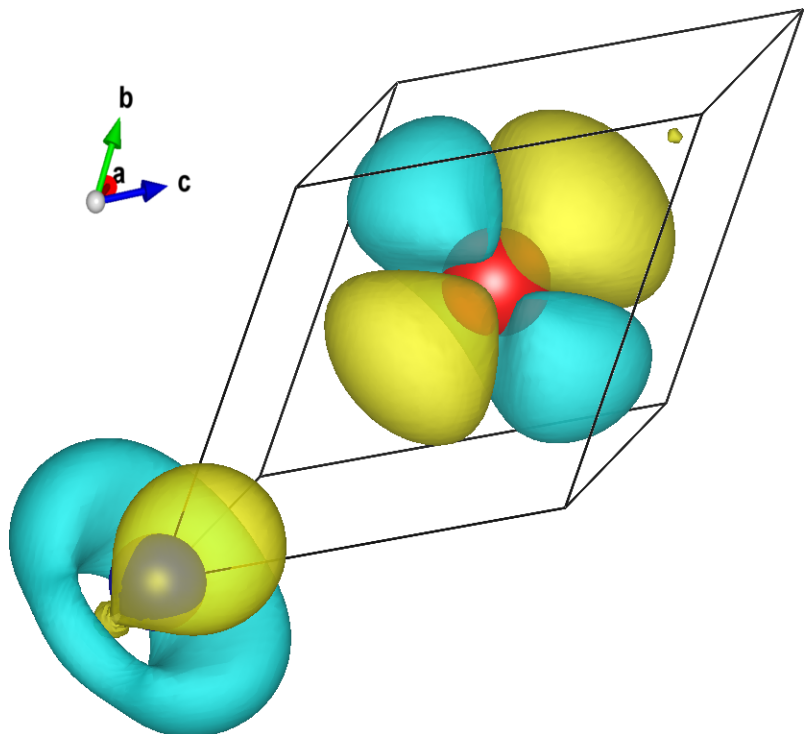


Figure 3.9: The variation of the charge density of the Bloch function of the first valence band $\frac{\partial|\psi(k)|^2}{\partial k}\Big|_{k=Z}$ away from Z towards A . Te and Ge ions are in red and blue, respectively. The charge asymmetry around Ge showcases the nonzero dipole moment along z , which couples to the local electric field near Ge ion.

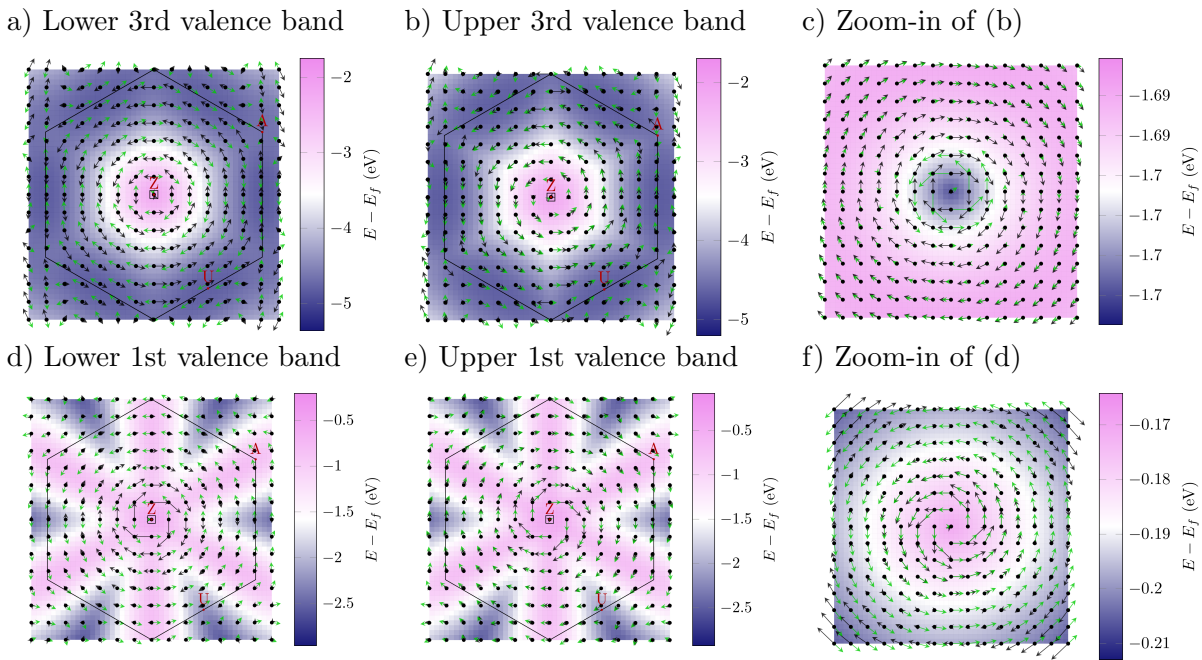


Figure 3.10: OAM and SAM textures around the Z point in the first and third valence bands of GeTe. The black and green arrows show the OAM and SAM textures, respectively. The length of the arrows was chosen separately for clarity in each figure and should thus not be compared. The color maps signify the energy of the bands, relative to the Fermi level. The small box around the Z point indicates the area, magnified in panels (c) and (f). In the zoomed figures (c) and (f) one can observe the change or relative orientation between the SAM and OAM when moving away from the Z point, signifying a change of character between $j = 1/2$ and $j = 3/2$.

Bibliography

- [1] Supriyo Datta and Biswajit Das. “Electronic analog of the electro-optic modulator”. In: *Applied Physics Letters* 56.7 (1990), pp. 665–667. ISSN: 00036951. DOI: 10.1063/1.102730.
- [2] Domenico Di Sante et al. “Electric control of the giant rashba effect in bulk gete”. In: *Advanced Materials* 25.4 (2013), pp. 509–513. ISSN: 09359648. DOI: 10.1002/adma.201203199.
- [3] Paolo Giannozzi et al. “QUANTUM ESPRESSO: a modular and open-source software project for quantum simulations of materials.” In: *Journal of physics. Condensed matter : an Institute of Physics journal* 21.39 (2009), p. 395502. ISSN: 0953-8984. DOI: 10.1088/0953-8984/21/39/395502.
- [4] Dongwook Go et al. “Surface orbitronics: new twists from orbital Rashba physics”. In: 1 (2016), pp. 1–8. ISSN: 2045-2322. DOI: 10.1038/srep46742. URL: <http://arxiv.org/abs/1611.04674> %0A <http://dx.doi.org/10.1038/srep46742>.
- [5] K Ishizaka. “Giant Rashba-type spin splitting in bulk BiTeI”. In: *Nature materials* 10.7 (2011), pp. 521–526. ISSN: 1476-1122. DOI: 10.1038/nmat3051. URL: <http://dx.doi.org/10.1038/nmat3051>.
- [6] T Jungwirth et al. “Antiferromagnetic spintronics”. In: *Nature Nanotechnology* 11.3 (2016), pp. 231–241. ISSN: 1748-3387. DOI: 10.1038/nnano.2016.18. URL: <http://www.nature.com/doifinder/10.1038/nnano.2016.18>.
- [7] Andrew D. Kent and Daniel C. Worledge. “A new spin on magnetic memories”. In: *Nature Nanotechnology* 10.3 (2015), pp. 187–191. ISSN: 1748-3387. DOI: 10.1038/nnano.2015.24. URL: <http://www.nature.com/doifinder/10.1038/nnano.2015.24>.

- [8] Minsung Kim et al. “Switchable $S = 1/2$ and $J = 1/2$ Rashba bands in ferroelectric halide perovskites.” In: *Proceedings of the National Academy of Sciences of the United States of America* 111.19 (2014), pp. 6900–4. ISSN: 1091-6490. DOI: 10.1073/pnas.1405780111. URL: <http://www.pnas.org/cgi/content/long/111/19/6900>.
- [9] J. Krempaský et al. “Surface versus bulk contributions to the giant Rashba splitting in the ferroelectric $\{\alpha\}$ -GeTe(111) semiconductor”. In: 111 (2015), pp. 1–10. DOI: 10.1103/PhysRevB.94.205111. URL: <http://arxiv.org/abs/1503.05004%0Ahttp://dx.doi.org/10.1103/PhysRevB.94.205111>.
- [10] Marcus Liebmann et al. “Giant Rashba-Type Spin Splitting in Ferroelectric GeTe(111)”. In: *Advanced Materials* 28.3 (2016), pp. 560–565. ISSN: 15214095. DOI: 10.1002/adma.201503459.
- [11] Arash A. Mostofi et al. “An updated version of wannier90: A tool for obtaining maximally-localised Wannier functions”. In: *Computer Physics Communications* 185.8 (2014), pp. 2309–2310. ISSN: 00104655. DOI: 10.1016/j.cpc.2014.05.003.
- [12] Seung Ryong Park et al. “Orbital-angular-momentum based origin of rashba-type surface band splitting”. In: *Physical Review Letters* 107.15 (2011), pp. 1–5. ISSN: 00319007. DOI: 10.1103/PhysRevLett.107.156803.
- [13] L. Petersen and P. Hedegård. “Simple tight-binding model of spin-orbit splitting of sp-derived surface states”. In: *Surface Science* 459.1 (2000), pp. 49–56. ISSN: 00396028. DOI: 10.1016/S0039-6028(00)00441-6.
- [14] K. M. Rabe and J. D. Joannopoulos. “Theory of the structural phase transition of GeTe”. In: *Physical Review B* 36.12 (1987), pp. 6631–6639. ISSN: 01631829. DOI: 10.1103/PhysRevB.36.6631.
- [15] Emmanuel Rashba and V. Sheka. “Symmetry of Energy Bands in Crystals of Wurtzite Type II . Symmetry of Bands with Spin-Orbit Interaction”. In: *Fiz. Tverd. Tela: Collected Papers* 2 (1959), pp. 162–76.